



New Development in Decarburization Research and Its Application to Spring Steels

Yisheng R. Chen¹ · Fan Zhang²

Received: 10 June 2023 / Revised: 27 July 2023 / Accepted: 4 August 2023 /
Published online: 26 August 2023

© The Author(s), under exclusive licence to Springer Science+Business Media, LLC, part of Springer Nature 2023

Abstract

Recently there was a new wave of research activities studying the decarburization behavior of spring steels with the main focus on the formation mechanism of a columnar ferrite layer within a certain temperature range which could not be explained by conventional decarburization theories. A new theory successfully developed recently in interpreting the oxide scale reduction mechanism on steel was then developed further and applied to interpret the observed columnar ferrite formation on spring steels. The essence of the new theory is that steel decarburization in the presence of a FeO scale on the steel surface is caused and governed by the reaction between the FeO scale and dissolved carbon in the steel, and therefore, the carbon concentration on the steel surface is determined by the FeO-steel interface equilibrium and cannot be treated as negligible within the temperature range where ferrite is able to form, because the equilibrium interface carbon concentration is in the same magnitude as the carbon solubility in ferrite. The new theory and available solutions for different decarburization scenarios using decarburization of 60Si2MnA as an example are summarized in this review. Explanations are given to interpret discrepancies between experimental observations and theoretical predictions. New areas for future research are also identified.

Keywords Spring steel · 60Si2MnA · Decarburization · FeO · Columnar ferrite formation · Austenite · Carbon diffusivity

✉ Yisheng R. Chen
yche6333@bigpond.net.au

Fan Zhang
fan.zhang@computherm.com

¹ Steel Research Australia, 20 The Crescent, Springvale, VIC 3171, Australia

² CompuTherm LLC, 8401 Greenway Blvd Suite 248, Middleton, WI 53562, USA

Introduction

There has been a long history of studies of steel decarburization [1–3]. In 1946, Pennington conducted a comprehensive study of carbon steel decarburization within the range of 691–927 °C in an atmosphere containing 20% H_2O – H_2 under which steel oxidation could not occur [3]. In that study, a ferrite ‘band’ was found to develop on the steel at 732–893 °C but not at 691 and 927 °C with a maximum ferrite thickness observed at 790–815 °C. Pennington attributed the decreased ferrite thickness toward 905 °C to the decreasing solubility of carbon in ferrite to zero at 905 °C. One limitation of Pennington’s analysis was that it was viewed that the carbon concentration in the ferrite formed was constant across the ferrite layer, and therefore, carbon diffusion in ferrite did not contribute to its growth.

The simultaneous oxidation and decarburization were studied by Birks and co-workers in 1970 [4–6]. Based on these studies, it was claimed that “the mechanism by which the decarburization of steels occur is well understood, particularly in the case of plain carbon and low alloy steels” [7]. However, the scope of Birks et al.’s studies was limited. First, the studies were focused on decarburization taking place in austenite only. No studies were directed to the situation where a ferrite layer could form. It was even claimed that as a result of the very low solubility of carbon in ferrite, the surface ferrite layer acted as a diffusion barrier, leading to much lower decarburization rate than that at temperatures above 910° [5, 8]. Secondly, while it was acknowledged that under an oxidizing atmosphere, decarburization took place via the reaction between the scale and dissolved carbon in the steel, Birks and co-workers continued to treat carbon concentration at the scale-steel interface as zero because of its low value. As will be demonstrated later, this assumption is acceptable only when decarburization takes place in the higher temperature range where the ferrite phase cannot form. Birks et al., citing Baud et al. [9], also claimed that a carefully produced FeO scale could protect steel from decarburization because CO or CO_2 could not escape through the FeO layer. As will be revealed in this study, this again is not true. Finally, alloying effects on steel decarburization had not been addressed by Birks et al.

Despite the claim that the mechanism of decarburization was already well understood [7], there has been a new wave of spring steel decarburization studies recently [10–26]. One reason for this was that when a spring steel was decarburized, a thick ferrite layer was always observed, same as that observed by Pennington [3] and there had been no consensus on the understanding of the mechanism governing its formation, and even on the temperature range where this ferrite layer could form. With the maximum ferrite thickness, some studies found that it occurred at 750 °C [11–16, 19, 21], some found at 800 °C, [22] some said 850 °C [17, 18, 20] and another one claimed that it was within 900–950 °C [25].

On another front, in our recent study of the reduction mechanism of oxide scale in pure nitrogen, it was found that dissolved carbon in a low carbon steel could react with the FeO scale, leading to both scale reduction and decarburization of the steel [27]. The discovery led to the development of not only a new scale reduction theory, but also a new decarburization theory as a result of direct reaction between the FeO scale and dissolved carbon in the steel.

Subsequently, the newly developed theory was applied to the study of decarburization of a commonly used spring steel 60Si2MnA [28–30]. The studies were assisted by a thermodynamic computation package, the Pandat™ program [31] and the PanFe data base [32] developed by CommuTherm. The current study provides an overview of the findings of these studies, summarized the key steps of the new decarburization theory, and demonstrate how to apply the theory and available solutions to predict and interpret decarburization behavior under different conditions.

Experimental Studies for the Steel Grade 60Si2MnA

The nominal compositions of two typical spring steel grades, 60Si2MnA and 55SiCr, are shown in Table 1. The 60Si2MnA steel examined in our recent studies contained Fe–0.602%C–1.787%Si–0.789%Mn–0.198%Cr. The 55SiCr grade contains a higher level of Cr and will be referred in this review for comparison.

Most of the previous experimental studies were conducted in ambient air with unknown moisture levels under isothermal conditions with the main objective to identify the ferrite formation temperature range and its formation mechanism. Moisture contents in the oxidizing gas can have a significant effect on silicon-containing steel oxidation [28, 33] and decarburization, which will be discussed when the issue arises.

Isothermal Oxidation Studies

Zhang et al. [13, 14] found that after oxidation in ambient air for 1.5 h, a columnar ferrite layer formed between 675 and 875 °C with a maximum thickness observed at 750 °C, as plotted in Fig. 1. Another study conducted in a N₂–2%O₂ gas by Liu et al. also found that the ferrite layer formed after holding at 750 °C for 30 min was greater than that at 800 °C, whereas a ferrite layer did not form at 850 °C [20, 34]. The absence of a ferrite layer at 850 °C was unusual. There must be other reasons, such as gas moisture levels, contributing to this.

Under similar oxidation conditions, Yu et al. however found that the maximum ferrite thickness was observed at 800 °C after 60 min of oxidation in ambient air, [22] as compared in Fig. 1. Zhao et al. also found a maximum ferrite thickness at 800 °C after oxidizing a 60Si2MnA steel in flowing air for 30 and 60 min [24]. On the other hand, in the study conducted by Y. Liu and X. Liu, very thick columnar ferrite layers were observed at 900–950 °C after oxidation in ambient air in a muffle furnace for 90 min [25]. This observation was unusual because formation of a pure ferrite layer at 950 °C is thermodynamically impossible, as will be discussed later.

Table 1 Typical compositions of two commonly used spring steel grades (wt%)

Element	C	Si	Mn	Cr	P	S	Balance
60Si2MnA	0.60	1.7	0.70	0.20	<0.02	<0.01	Fe
55SiCr	0.55	1.50	0.70	0.70	<0.02	<0.01	Fe

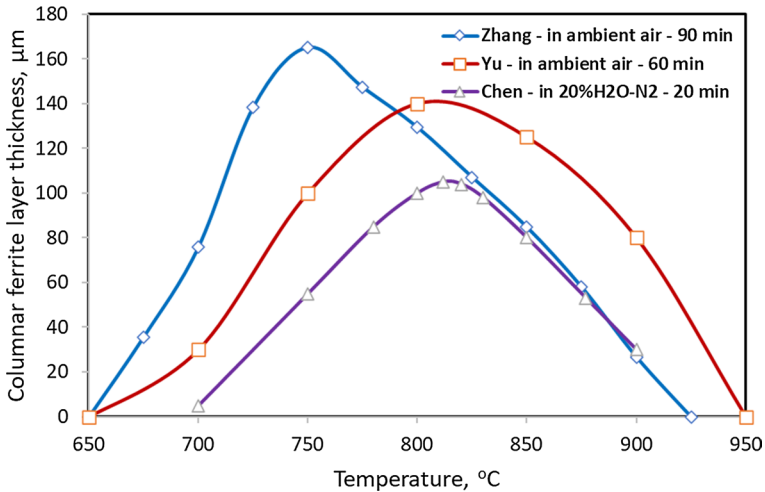


Fig. 1 Columnar ferrite formation on 60Si2MnA after oxidation and decarburization observed in different studies. Data sources are from Zhang et al. [13, 14], Yu et al. [22], and Chen et al. [28]

Recently we examined the decarburization behavior of 60Si2MnA in an atmosphere containing 20%H₂O-N₂ at 700–900 °C [28]. A scale layer of less than 6 μm formed on the surface because the gas was not severely oxidizing. A columnar ferrite layer was observed within the range of 750–900 °C, but not at 700 °C, as plotted in Fig. 1. Some ferrite morphologies are shown in Fig. 2. It can be seen that the maximum ferrite thickness developed within 800–820 °C, consistent with the results obtained by Yu et al. [34] and Zhao et al. [24].

Mechanism of Forming the Columnar Ferrite Structure

Apart from the similar patterns of forming a maximum ferrite thickness at about 800 °C, the microstructures of the ferrite layers observed on 60Si2MnA were also similar to those observed by Pennington on a high carbon steel [3], with the ferrite

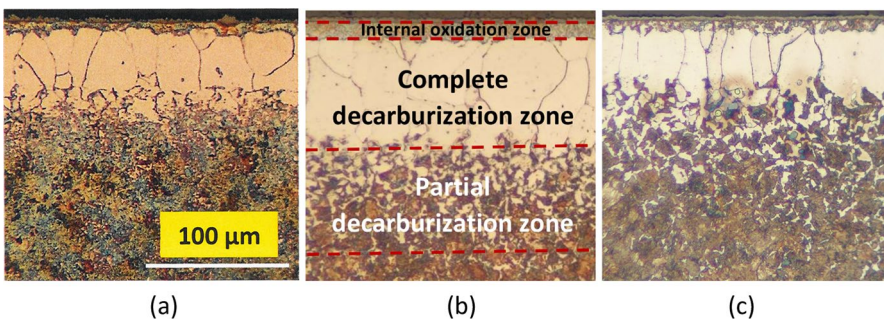


Fig. 2 Typical columnar ferrite layers formed after isothermal holding in a 24.8H₂O-N₂ gas for 20 min at **a** 750 °C, **b** 830 °C, and **c** 877 °C [28]

grains growing in a columnar structure spanning across the entire ferrite layer, as seen in Fig. 2 as compared to the images presented by Pennington reproduced in Fig. 3.

The development of this ferrite layer at 760, 788, 816, 871 °C was explained by Pennington with the assistance of an early binary Fe–C diagram and that at 760 °C as an example. Within the $\alpha + \gamma$ zone at this temperature, the equilibrium carbon concentrations in the ferrite and austenite were 0.026% and 0.50%, respectively (note that the more correct compositions should be 0.016% and 0.54% at 760 °C as calculated using Pandat™). While the steel was decarburized, there was a local equilibrium at the steel-gas interface to take away carbon from the steel surface. The surface carbon content was then decreasing continuously from initially 0.85% toward 0.50%. Once the surface concentration reached 0.50%, it could no longer decrease gradually, but dropped all the way to 0.026% to form a thin ferrite layer.

Pennington did not explain why the ferrite grains developed into a columnar shape, but judging from the morphology observed, after the formation of ferrite nuclei on the austenite surface, the continuous growth must have been taking place via a directional ferrite growth mechanism, opposite to the carbon diffusion direction through the ferrite layer, thus developing into a columnar structure, similar to that developed under directional annealing of very low carbon steels, [35] or the columnar zone developed in an ingot where directional solidification took place [36].

Decarburization in the Absence of a Columnar Ferrite Layer (at $T > 900$ °C)

When the decarburization temperature is sufficiently high, the decarburization zone shows a different structure, as shown in Fig. 4 [37]. Generally, there is a complete decarburization zone near the steel surface (Fig. 4b) where only light gray ferrite grains are visible. The morphology of this zone is different from the columnar ferrite structure formed within the range of 700–900 °C. At higher temperatures, this zone is in an austenitic state, containing very little carbon. It transforms to equiaxed

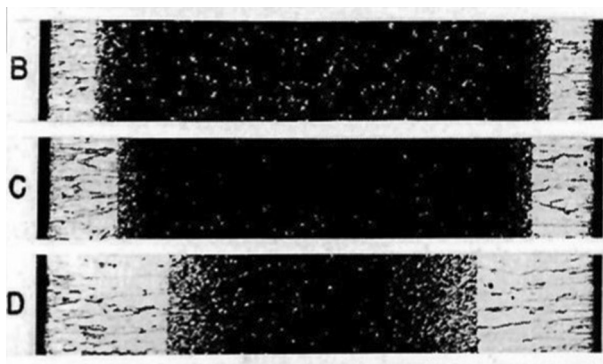


Fig. 3 Columnar ferrite structure developed on a high carbon steel (0.85wt%C–0.17%Mn–0.26%Si) in 20% H_2O – H_2 at 816 °C for 1, 2, and 6 h (B, C, and D, respectively) [3]

ferrite grains during cooling. Under this zone, there is a partial decarburization zone comprising a mixture of light gray ferrite grains and dark gray pearlite colonies. The depth of the partial decarburization is estimated by locating a zone where the light gray ferrite grains started to disappear. The estimated depths of the complete decarburization and partial decarburization zones developed at different temperatures are shown in Fig. 5. The corresponding consumptions of steel by oxidation at different temperatures are also shown in Fig. 6 [37].

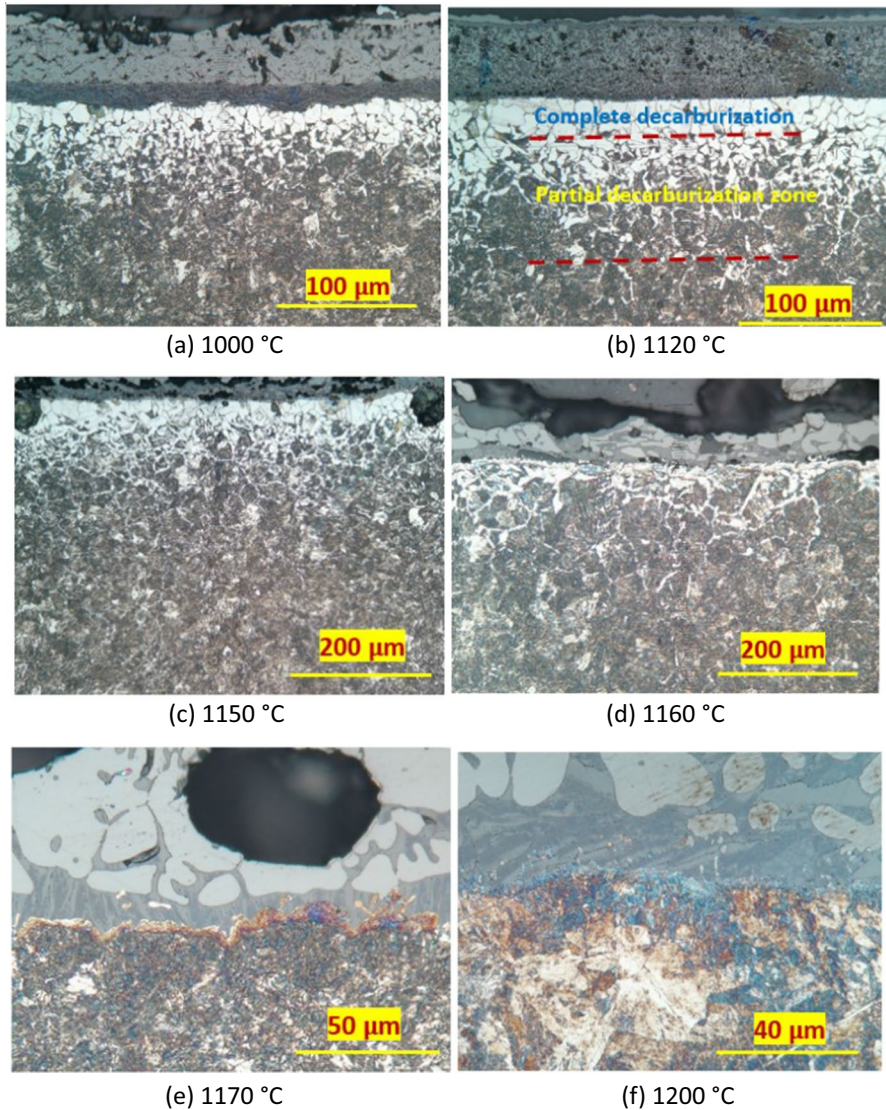


Fig. 4 Decarburization zones formed after isothermal holding for 20 min in air-24.8% H_2O at 1000–1200 °C [30, 37]: **a** 1000 °C, **b** 1120 °C, **c** 1150 °C, **d** 1160 °C, **e** 1170 °C and **f** 1200 °C

As compared to steel consumptions, several observations of the decarburization tendency can be made. First, there is a steady increase of the total decarburization depth from 100 μm to 165 μm within the range of 1000–1120 $^{\circ}\text{C}$ (Fig. 5), corresponding to a steady increase in steel consumption from 70 μm at 1000 $^{\circ}\text{C}$ to 150 μm at 1120 $^{\circ}\text{C}$ but then the steel consumption rate stays about the same within 1120 $^{\circ}\text{C}$ –1150 $^{\circ}\text{C}$ (Fig. 6) while the decarburization depth continues to increase to about 180 μm at 1150 $^{\circ}\text{C}$. Second, corresponding to the rapid increase in the amount of steel consumption beyond 1150 $^{\circ}\text{C}$ (Fig. 6), the decarburization zone depth on the contrary reduced significantly at 1160 $^{\circ}\text{C}$ (Fig. 4d) and then to zero at 1170 $^{\circ}\text{C}$ (Figs. 4e and 5). Finally, beyond 1170 $^{\circ}\text{C}$, the decarburization zone disappeared altogether, while the steel consumption rate increased rapidly (Figs. 4f, 5 and 6).

Judging from the morphologies, the steel surface is covered by a molten oxide phase at temperatures above 1160 $^{\circ}\text{C}$ [30].

The disappearance of the decarburization zone at temperatures above 1170 $^{\circ}\text{C}$ is consistent with the observations by Y. Liu et al. [20] and J. Liu et al. [26]

Development of the New Decarburization Theory

Direct Reaction Between Dissolved Carbon and FeO Scale

A study was conducted recently to understand the reason why there was always a weight loss when a hot-rolled low carbon steel was heated in high purity nitrogen [27]. At the reaction temperatures, the scale had a wustite structure. After holding at a temperature within the range of 600–900 $^{\circ}\text{C}$, different degrees of scale reduction

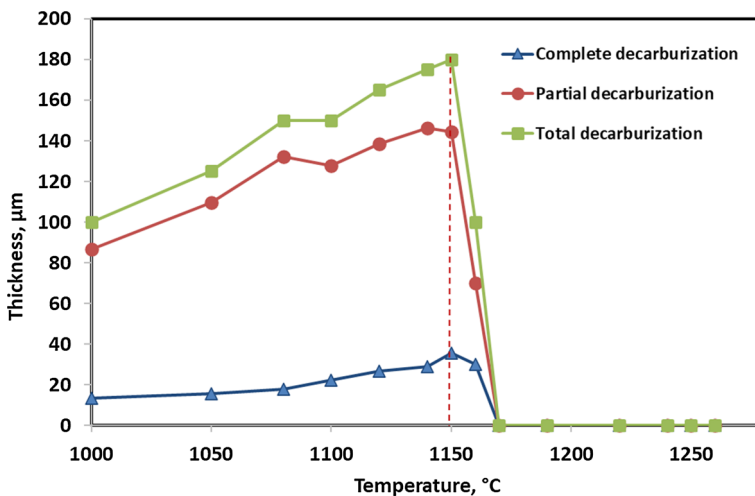


Fig. 5 Measured total decarburization depths as a function of oxidation temperature after isothermal holding for 20 min in air-24.8% H_2O [37]

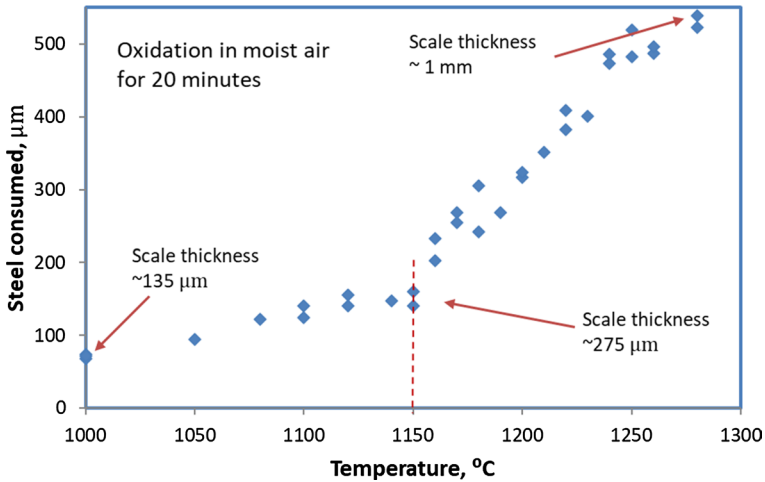


Fig. 6 Amount of steel consumed as a function of oxidation temperature after isothermal holding for 20 min in air-24.8% H_2O [30, 37]

were observed, as shown Fig. 7a. The reduction kinetics initially followed the parabolic law but then deviated at longer times.

Examination of the scale structure and the steel substrate revealed that while the scale was reduced (Fig. 7b), the steel substrate underneath was decarburized (Fig. 7c, d). Reduction of the scale generated porosities at the interface, but the outer region remained compact and continuous, as seen in Fig. 7b. After 3 h of reaction at 800 °C, the entire specimen was decarburized [27]

Because the steel surface was covered by a compact scale, which was reduced gradually over time, there was only one mechanism that could be responsible for the observed decarburization phenomenon, which was the direct reaction between the FeO scale and dissolved carbon in the steel. Generation of numerous porosities did not stop the decarburization process.

Our observations are consistent with the findings of another study by Pennington [38]. In that study, a number of pickled and unpickled steel specimens were stacked alternately with spacings between them and then isothermally heated in an enclosed chamber at 788 °C for 28 h. The gas volume generated by the reactions taking place between the specimens and the atmosphere in the chamber was then carefully measured and the remaining carbon contents in both sets of specimens were analyzed.

The theory behind the experiments was that if the remaining O_2 in the chamber reacted with dissolved carbon in the steel to form CO_2 , one O_2 molecule would generate one CO_2 molecule without causing gas expansion. However, if CO_2 reacted with dissolved carbon again to form CO , then one CO_2 molecule would generate two CO molecules, thus causing gas expansion. The increase of the gas volume then could be measured and recorded over time to monitor the kinetics of reaction. The specimens after the treatment could then be analyzed for carbon losses.

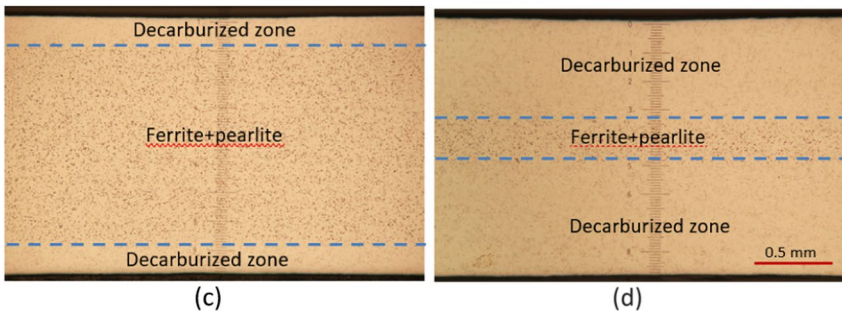
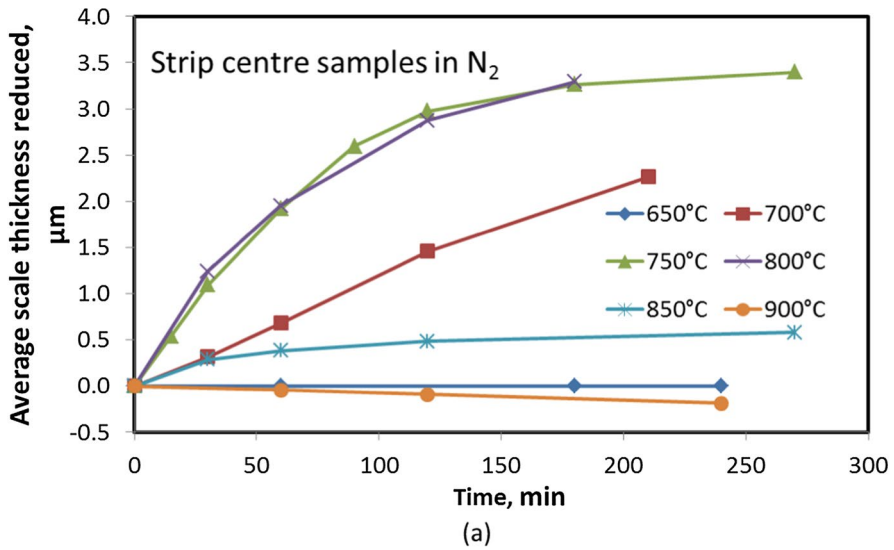


Fig. 7 FeO-steel reaction during isothermal holding in high purity N₂ causing decarburization of a low carbon steel (0.055%C–0.23%Mn–<0.005%Si): **a** scale reduction kinetics at 650–900 °C, **b** scale-steel interface after holding for 60 min, **c** decarburization zone in the steel after holding for 30 min; **d** decarburization zone in the steel after holding for 90 min at 800 °C [27]

The experiments convincingly demonstrated that decarburization reactions took place over a period of 16 h and the remaining carbon contents in both the scaled and pickled samples were reduced from the original 0.062wt% to 0.010wt% [38].

Therefore, the oxide reduction kinetics shown in Fig. 7a directly represented the kinetics of reaction between the FeO scale and dissolved carbon in the steel. Several

observations can be made from Fig. 7a. First, the reaction between dissolved carbon with the scale was possible at 700–850 °C. Second, there is a maximum rate observed at 750 and 800 °C, which was followed by that at 700 °C and then at 850 °C. Third, no reaction took place at 650 °C and finally, there was in fact a small weight gain at 900 °C, which was recognized as the result of oxidation of the steel by residual oxygen and water vapour in the nitrogen gas used.

Based on above observations and analyses, a theory was developed to interpret the scale reduction and decarburization phenomena. The theory was based on the propositions that (a) the reaction between the scale and the dissolved carbon in the steel could only proceed if the solubility of carbon in the matrix phase, being ferrite at 659–859 °C for the steel examined (Fe–0.055%C–0.23%Mn) as will be shown later, was greater than the carbon concentration at the FeO–steel interface, (b) the carbon concentration at the FeO–steel interface is determined by the local equilibrium achieved at the scale–steel interface, and (c) the reaction products CO₂ and CO could escape through the FeO scale layer even when the FeO layer was compact and continuous, as discussed elsewhere [27]. Based on these propositions, the proposed reaction takes place via the following steps.

First, it is assumed that when the FeO scale reacts with dissolved carbon [C] in the steel,

both CO and CO₂ are produced:



The CO and CO₂ gases then maintain a local equilibrium with FeO and the steel:



Using available thermodynamic data in the literature [39, 40], the standard Gibbs free energy of formation for Reaction (3) is given by:

$$\Delta G_{(3)}^o = -22800 + 24.267 T \text{ (J/mole of CO)} \quad (4)$$

When the reaction (3) reaches equilibrium:

$$\frac{P_{CO}}{P_{CO_2}} = \exp\left(\frac{-22800 + 24.267 T}{RT}\right) \quad (5)$$

The $\frac{P_{CO}}{P_{CO_2}}$ thus obtained can be used as the second step to determine the equilibrium carbon activity at the interface assuming $P_{CO} + P_{CO_2} = 1$ atm if the experiments are conducted under ambient pressure from the following reaction:



The standard Gibbs free energy of formation for this reaction is given by: [39, 40]

$$\Delta G_{(6)}^{\circ} = -RT \ln \left[\frac{P_{\text{CO}}^2}{a_c P_{\text{CO}_2}} \right] = 170700 - 174.5T \quad (\text{J/mole of C}) \quad (7)$$

where a_c is the equilibrium carbon activity at the FeO-steel interface with graphite being the standard state. From Eq. (7), we obtain:

$$a_c = \frac{P_{\text{CO}}^2}{P_{\text{CO}_2}} \exp \left[\frac{(170700 - 174.5 T) \left(\frac{\text{J}}{\text{mole of C}} \right)}{RT} \right] \quad (8)$$

After the equilibrium carbon activity is determined, the corresponding carbon concentration in the steel at the scale-steel interface can be calculated using known relationships between carbon activities and carbon concentrations as the third step.

For dissolved carbon in α -Fe, the relationship to express the activity coefficient of carbon in ferrite for carbon steel, $Y_C(\text{ferrite})$, is given by Lobo and Gaiger: [41]

$$\log Y_C(\text{ferrite}) = \log \left(\frac{a_C}{X_C} \right) (\text{ferrite}) = \frac{5846}{T(\text{K})} - 2.687 \quad (9)$$

where X_C is the equilibrium molar fraction of carbon in the steel matrix at the scale-steel interface, which can be converted to carbon concentration in weight percent.

The carbon solubilities in the ferrite phase of the experimental steel Fe–0.055%C–0.23%Mn, calculated using PandatTM [31] and the PanFe [32] database were then plotted in Fig. 8 as the fourth step for the determination of reaction possibility. For comparison and later use, the carbon solubilities in ferrite for 60Si2MnA and 55SiCr, also obtained from PandatTM and PanFe are plotted in Fig. 8.

It can be seen that while the equilibrium carbon concentration at the steel surface is very low (<0.01%), it is not negligible as compared to the solubilities of carbon in ferrite, and more importantly, it can be used to assess within what temperature range where the dissolved carbon in the ferrite phase can react with the adjacent FeO scale. It can also be used to determine whether a ferrite layer can develop on a steel when the steel is being decarburized, such as that shown in Fig. 7c, d.

For the Fe–0.055%C–0.23%Mn steel, it can be seen from Fig. 8 that the carbon solubilities within the range of 659 °C to 859 °C are greater than the calculated interface equilibrium carbon concentration, but smaller outside this range. This explains the reason why the FeO scale could react with dissolved carbon in the steel at 700–850 °C, but not at 650 °C and 900 °C, as seen in Fig. 7a, if the steel is a ferritic state.

Figure 8 also shows that there is a maximum difference between the carbon solubility in the ferrite phase and the equilibrium carbon concentration at the interface at about 720 °C. However, the maximum scale reduction or decarburization rate was not observed at 720 °C in Fig. 7a. The reason for this was that the rate of decarburization was also affected by the carbon diffusivity in the ferrite phase.

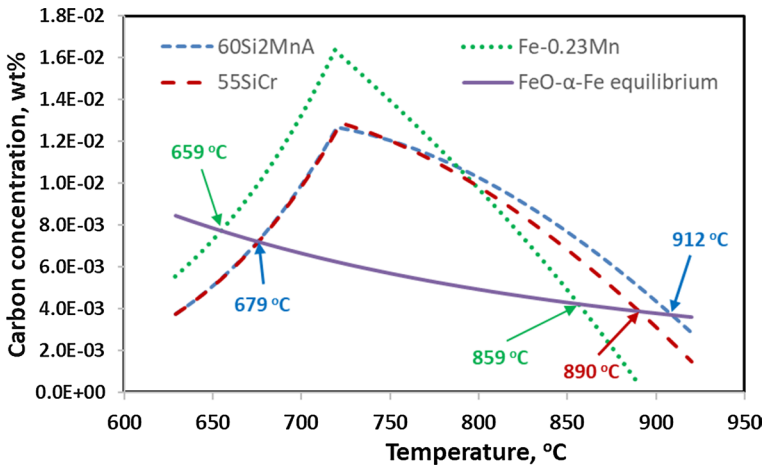


Fig. 8 Calculated carbon concentration at the FeO-steel interface as a function of temperature (solid line), as compared with the carbon solubilities (dotted and dashed lines) in ferrite calculated using Pandat™ [31] and PanFe [32] to determine the possibility of reaction between the FeO scale and dissolved carbon in ferrite adjacent to the FeO scale

To represent the combined effect of the concentration difference and diffusivity, the concept of carbon permeability ($P_C^{\alpha-Fe}$) through the ferrite layer was introduced as the fifth step [42]:

$$P_C^{\alpha-Fe} = D_C^{\alpha-Fe} \cdot (C_C^{\alpha-Fe/Bulk} - C_C^{\alpha-Fe/FeO}) = D_C^{\alpha-Fe} \cdot \Delta C_C^{\alpha-Fe} \tag{10}$$

where $D_C^{\alpha-Fe}$ is the diffusion coefficient of carbon through the ferrite layer, $C_C^{\alpha-Fe/Bulk}$ is the equilibrium carbon concentration on the ferrite side at the interface between the ferrite layer and the bulk of steel in wt%, $C_C^{\alpha-Fe/FeO}$ is the equilibrium carbon concentration in ferrite at the steel-scale interface in wt%, and $\Delta C_C^{\alpha-Fe}$ is the carbon concentration difference between the two interfaces of the surface ferrite layer.

When the ferrite layer is thin, the carbon concentration gradient in the ferrite layer is approximately linear and the carbon flux $J_C^{\alpha-Fe}$ flowing through the ferrite layer can be expressed as:

$$J_C^{\alpha-Fe} = A \cdot D_C^{\alpha-Fe} \cdot \frac{\Delta C_C^{\alpha-Fe}}{X} = A \cdot \frac{P_C^{\alpha-Fe}}{X} \text{ moles cm}^{-2} \text{ s}^{-1} \tag{11}$$

where A is a constant used to convert the concentration of carbon from wt% to mole/cm³ and X is the thickness of the ferrite layer in cm. The calculated carbon permeability as a function of temperature, using the carbon concentrations shown in Fig. 8 and the carbon diffusivities shown in Fig. 9a, derived from the work of Smith [42], for the Fe–0.055%C–0.23%Mn steel at 650–850 °C are shown in Fig. 9b. It is seen that the calculated permeabilities for the several experimental temperatures match the observed scale reduction and hence steel decarburization rate very well, with the maximum rate observed within the range of 750–800 °C, followed by that at 700 °C, then by a very low rate at 850 °C, and finally a zero rate at 650 °C.

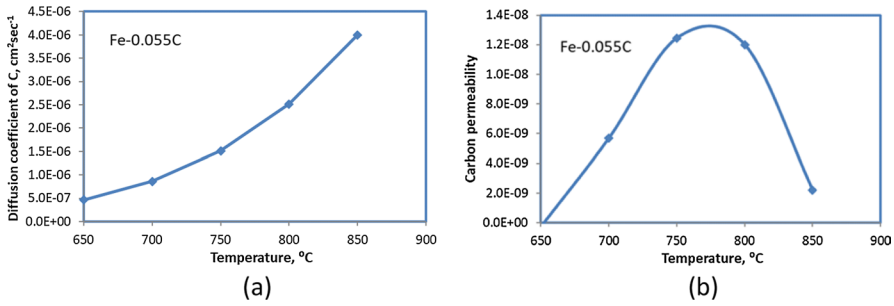


Fig. 9 **a** Diffusivity of carbon in ferrite [42] and **b** carbon permeability through the ferrite layer within the range where FeO can reaction with dissolved carbon in the steel, as shown in Fig. 8

Thus, the combined effect of the carbon concentration difference $\Delta C_C^{\alpha-Fe}$ which has a maximum value at about 720 °C and the carbon diffusivity in ferrite $D_C^{\alpha-Fe}$ which increases monotonically with temperature shifted the most rapid decarburization temperature to one within the range of 750–800 °C for the Fe–0.055%C–0.23%Mn steel.

It will be demonstrated later that the same mechanism is responsible for the development of a maximum columnar ferrite layer thickness at a certain temperature for the spring steel 60Si2MnA examined. Because the temperature range where the carbon solubility in ferrite is greater than the equilibrium carbon concentration at the FeO-ferrite interface is shifted higher to 679–912 °C for 60Si2MnA, as shown in Fig. 8, this maximum ferrite thickness temperature is expected to be greater than the most rapid decarburization temperature observed for the Fe–0.055%C–0.23%Mn steel.

Finally, the A₃ line for the Fe–C–0.23%Mn system was computed using Pandat™ and PanFe, as shown in Fig. 10. It is seen that the Fe–0.055%C–0.23%Mn steel was in fact in an austenitic state at 900 °C.

In order to determine whether the dissolved carbon in the austenitic steel could be reacting with the scale, the interface carbon activity calculated from Eq. (8) was converted to the equilibrium carbon concentration in austenite using the equation given by Ellis et al. [43]

$$\log a'_C = \log \left[\frac{X'_C}{1 - 5X'_C} \right] + \frac{2080}{T} - 0.639 \tag{12}$$

where X'_C is the molar fraction of carbon in austenite. The results thus obtained were converted to wt% and shown in Fig. 10. It is seen that at 900 °C, the equilibrium carbon concentration at the interface is essentially identical to the carbon concentration in the steel. Therefore, Reactions (1)–(3) and (6) could not proceed at this temperature. This provides a satisfactory explanation for the observation that the FeO scale could not react with dissolved carbon in the steel at 900 °C as shown in Fig. 7a.

The theory detailed above thus provides perfect interpretation of the observed reactions between the FeO scale on the steel surface and the dissolved carbon in

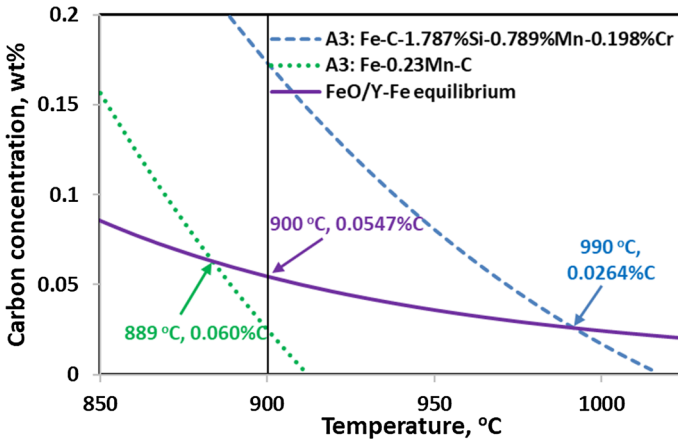


Fig. 10 Equilibrium carbon concentration at the scale-steel interface assuming that the steel phase in equilibrium is austenite, as compared to the high temperature ends of the A_3 lines obtained from Fe–C–1.787%Si–0.789%Mn–0.198%Cr and Fe–C–0.23%Mn isopleths

the Fe–0.055%C–0.23%Mn steel, leading to simultaneous scale reduction and steel decarburization. The principles then can be applied to the study of decarburization of other steels.

Application of the New Theory to Decarburization of 60Si2MnA

As shown in Table 1, spring steels generally contain a much higher level of carbon (0.4–0.6%), a significant amount of silicon (1.5–2.0%) and various levels of Cr and Mn. As shown in Figs. 8 and 10, the alloying elements affect the temperature range of ferrite formation, carbon solubilities in ferrite, and the position of the A_3 lines. For example, for the 60Si2MnA steel, formation of a columnar ferrite layer is thermodynamically impossible at temperature above 912 °C because the carbon solubilities at temperatures above 912 °C are below the equilibrium carbon concentrations at the FeO-ferrite interface, whereas for the 55SiCr steel, the critical temperature was at 890 °C.

However, ferrite formation is still possible in the 60Si2MnA steel examined (Fe–0.602%C–1.787%Si–0.789%Mn–0.198%Cr) at temperatures above 912 °C until the temperature exceeds 1025 °C, but only as a component of a mixture with austenite if the carbon concentration in the surface layer is lowered to that under the A_3 line shown in Fig. 10, as also shown in the isopleth computed using Pandat™ and PanFe in Fig. 11a.

As shown in Figs. 8 and 10, when the 60Si2MnA steel is decarburized by the FeO scale, the equilibrium interface carbon concentration does not reduce to zero, whether the steel is in a ferritic or austenitic state within the range of 600–1050 °C. When a single-phase columnar ferrite forms at $T = 679–912$ °C, the interface carbon concentration is purely determined by Eq. (9) and Fig. 8. When a single-phase

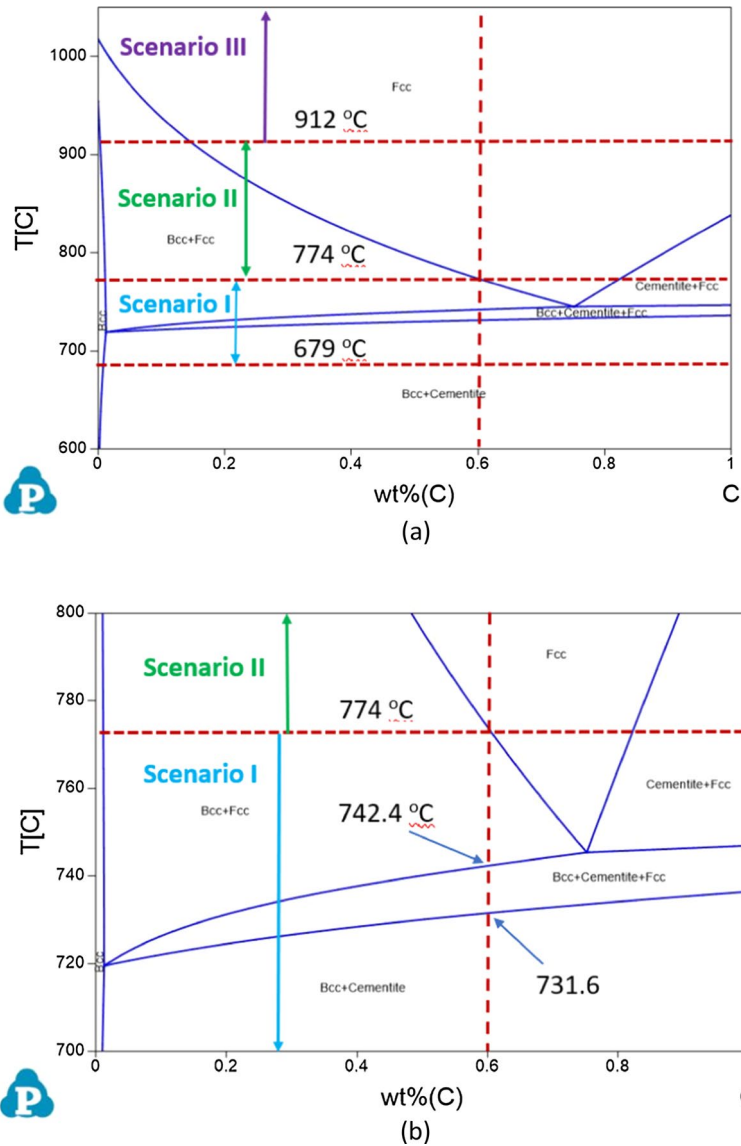


Fig. 11 Temperature zones where three different decarburization scenarios are operating: **a** full isopleth of the Fe-C-1.787%Si-0.789%Mn-0.198%Cr, **b** enlarged section for 700–800 °C of the Fe-C-1.787%Si-0.789%Mn-0.198%Cr isopleth

austenite forms at temperatures above 990 °C, the interface composition is purely determined by Eq. (12) and Fig. 10. Between 912 and 990 °C, neither a single ferrite phase nor austenite phase can form on the surface of the steel. Therefore, within the temperature range of 912 °C and 990 °C, when the carbon concentration in the surface layer of the steel is decreased to that lower than the A_3 value shown in Fig. 10,

there will be a two-phase ferrite–austenite structure developed on the steel surface, in equilibrium with the carbon activity determined by Eq. (8) with the concentrations of the ferrite and austenite determined by Eqs. (9) and (12) or Figs. 8 and 10, respectively. This is a situation that had not been dealt with in previous studies. In this review, this will be treated as a situation where carbon diffusion takes place in austenite only due to two reasons. First, the austenite phase is continuously present from the bulk to the interface. Second, the rate of carbon diffusion is much more rapid in ferrite. Therefore, it is assumed that the presence of a ferrite phase in the surface layer does not impede on carbon transport from the bulk to the interface.

Based on above discussions, the three scenarios of carbon diffusion in the steel during decarburization of a 60Si2MnA steel can be marked in Fig. 11a and schematically shown in Fig. 12, assuming no redistribution of the alloying elements during ferrite growth, namely under the para-equilibrium conditions [44].

Scenario I—at $T = 679\text{ }^{\circ}\text{C} - 774\text{ }^{\circ}\text{C}$:

The bulk of steel is a mixture of two-phase $\alpha\text{-Fe} + \gamma\text{-Fe}$ at $742.4 - 774\text{ }^{\circ}\text{C}$, $\alpha\text{-Fe} + \text{Fe}_3\text{C}$ at $T < 731.6\text{ }^{\circ}\text{C}$, and three-phase $\alpha\text{-Fe} + \gamma\text{-Fe} + \text{Fe}_3\text{C}$ state at $731.6 - 742.4\text{ }^{\circ}\text{C}$, as shown more clearly in Fig. 11b. The carbon concentration in the bulk equals to the original carbon concentration $C_{\text{bulk}} = 0.602\text{ wt}\%$. The carbon concentration in ferrite at the ferrite–bulk interface is equal to the carbon concentration of the $\alpha\text{-Fe}$ phase in the bulk, $C_{\alpha}^* = C_{\alpha\text{in bulk}}$. The carbon concentration in ferrite at the FeO–ferrite phase is determined by the simultaneous equilibria of the interface Reactions (1)–(3) and (6), as also indicated in Fig. 12a.

Scenario II—at $T = 774 - 912\text{ }^{\circ}\text{C}$:

The carbon concentration in the bulk equals to the original carbon concentration, $C_{\text{bulk}} = 0.602\text{ wt}\%$. Carbon concentrations in austenite and ferrite at the $\alpha\text{-}\gamma$ interface, C_{γ}^* and C_{α}^* , respectively, are determined by the equilibrium between the two phases, assuming no re-distribution of the alloying elements. The carbon concentration in ferrite at the FeO–ferrite interphase is determined by the simultaneous equilibria of the interface reactions as indicated, namely via Reactions (1)–(3) and (6).

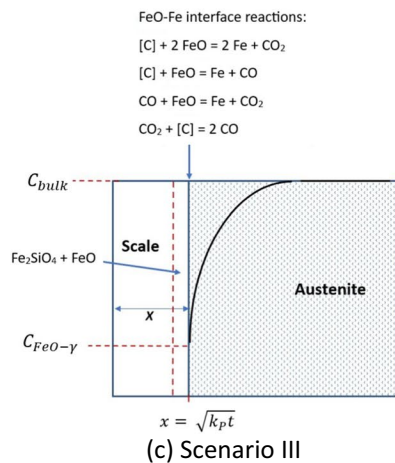
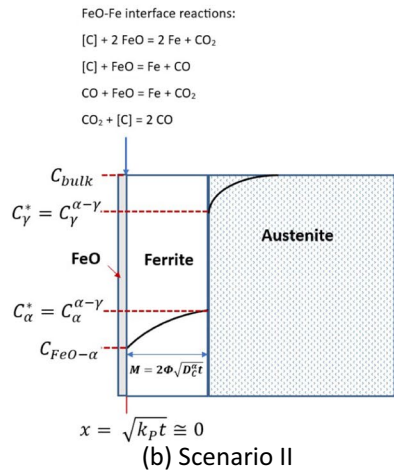
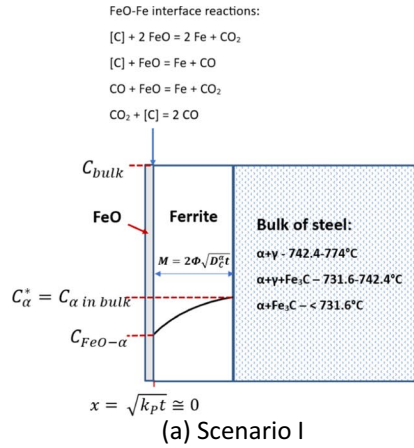
Scenario III—at $T > 912\text{ }^{\circ}\text{C}$:

The carbon concentration in the bulk equals to the original carbon concentration, $C_{\text{bulk}} = 0.602\text{ wt}\%$. The equilibrium carbon concentration in austenite at the FeO–steel interface, $C_{\text{FeO-S}}$, is determined by the simultaneous equilibria of the listed reactions at the interface, namely, Reactions (1)–(3) and (6).

3. Analytical Solutions

Analytical solutions are obtained by solving Fick's second law. The general solution under the assumption that the carbon diffusivity D is not concentration dependent:

Fig. 12 Three different decarburization scenarios as marked in Fig. 11a, showing different diffusion processes involved: **a** Scenario I, **b** Scenario II, and **c** Scenario III



$$C_{x,t} = A + B \cdot \operatorname{erf} \left[\frac{x}{2\sqrt{D \cdot t}} \right] \quad (13)$$

where the parameters A and B are determined by specific initial and boundary conditions.

Decarburization of spring steels generally takes place together with steel oxidation. The only scenario where an analytical solution is available under simultaneous oxidation and decarburization conditions is Scenario III where carbon diffusion takes place within austenite only with only one moving scale-steel interface. For the other two scenarios with two moving interfaces involved, analytical solutions could only be obtained under the condition that the movement of the scale-steel interface is negligible, namely $x = \sqrt{k_p t} \cong 0$, as indicated in Fig. 12a, b, where k_p is the rate constant of steel oxidation [45].

Analytical Solution for Scenario I

In Scenario I, the bulk of steel is always in a two-phase or three-phase state. We only need to consider diffusion in the surface ferrite layer, as shown in Fig. 12a. Following the procedure Wagner used, [46] the carbon concentration as a function of the distance through the ferrite layer and time is expressed as:

$$C_{x,t} = C_{\text{FeO}-\alpha} + \frac{C_{\alpha}^* - C_{\text{FeO}-\alpha}}{\operatorname{erf}(\Phi)} \operatorname{erf} \left(\frac{x}{2\sqrt{D_C^{\alpha} \cdot t}} \right) \quad (14)$$

where C_{α}^* is the carbon concentration in ferrite at the interface between the ferrite layer and the bulk of steel and is equal to the ferrite carbon concentration in the bulk $C_{\alpha}^* = C_{\alpha \text{ in bulk}}$, D_C^{α} is the diffusivity of carbon in ferrite, Φ is a dimensionless parameter at a given temperature, determined by:

$$F(\Phi) = \sqrt{\pi} \times (C_{\text{bulk}} - C_{\alpha}^*) - \frac{C_{\alpha}^* - C_{\text{FeO}-\alpha}}{\Phi e^{\Phi^2} \operatorname{erf}(\Phi)} = 0 \quad (15)$$

Once the Φ meeting Eq. (15) is found, the ferrite layer thickness, M , can be calculated using the following equation:

$$M = 2\Phi \sqrt{D_C^{\alpha} \cdot t} \quad (16)$$

Equation (15) had been then simplified by Smith to become the permeability equation:

$$P_C^{\alpha-\text{Fe}} = D_C^{\alpha} C_{\alpha}^* = \frac{\left(C_{\text{bulk}} - \frac{2}{3} C_{\alpha}^* \right)}{2} \times \frac{M^2}{t} \quad (17)$$

or

$$M = \sqrt{\frac{6 \cdot C_{\alpha}^* \cdot D_C^{\alpha} \cdot t}{3C_{\text{bulk}} - 2 \cdot C_{\alpha}^*}} \tag{18}$$

Equation (18) will be called the Smith’s equation, or Smith’s permeability equation. In deriving this equation, Smith had assumed that the surface carbon concentration was negligible, *i.e.* $C_s \cong 0$. It had been the equation used by many researchers to calculate the ferrite layer thickness caused by decarburization in their studies [10, 19, 21, 47, 48]. Because it had been simplified from Eq. (15), it can only be used to calculate ferrite thickness under Scenario I conditions, where only carbon diffusion through the ferrite layer contributes to the growth of the ferrite layer.

If however, the carbon concentration on the surface is not negligible, namely $C_s \neq 0$, Eq. (17) then takes the form of:

$$P_C^{\alpha\text{-Fe}} = D_C^{\alpha} (C_{\alpha}^* - C_s) = \frac{\left(C_{\text{bulk}} - \frac{2}{3}C_{\alpha}^*\right)}{2} \times \frac{M^2}{t} \tag{19}$$

and Eq. (18) becomes:

$$M = \sqrt{\frac{6 \cdot (C_{\alpha}^* - C_{\text{FeO-}\alpha}) \cdot D_C^{\alpha} \cdot t}{3C_{\text{bulk}} - 2 \cdot C_{\alpha}^*}} \tag{20}$$

This equation will be called the modified Smith’s equation to be used under the conditions where the interface carbon concentration is not negligible.

Analytical Solution for Scenario II

In this scenario, two diffusion processes are contributing to the formation of the ferrite layer, as shown in Fig. 12b. Carbon diffusion through the ferrite layer leads to its own thickening, whereas carbon diffusion from the bulk of the steel to the ferrite–austenite interface tends to slow down the thickening of the ferrite layer.

As the boundary conditions for the ferrite layer growth are the same at all temperatures, except that now $C_{\alpha}^* = C_{\alpha}^{\alpha-\gamma}$, regardless of whether carbon diffusion in the austenite contributes to the ferrite growth or not, the carbon concentration in the ferrite layer can still be described by Eq. (14) but takes the form of,

$$C_{x,t}^{\alpha} = C_{\text{FeO-}\alpha} + \frac{C_{\alpha}^{\alpha-\gamma} - C_{\text{FeO-}\alpha}}{\text{erf}(\Phi)} \text{erf}\left(\frac{x}{2\sqrt{D_C^{\alpha} \cdot t}}\right) \tag{21}$$

after replacing C_{α}^* with $C_{\alpha}^{\alpha-\gamma}$. Following the procedure described by Wagner [46] the carbon concentration in austenite as a function of distance and time can be expressed as:

$$C_{x,t}^{\gamma} = C_{\text{bulk}} - \frac{C_{\text{bulk}} - C_{\gamma}^{\alpha-\gamma}}{\operatorname{erfc}\left(\frac{\Phi}{\beta}\right)} \operatorname{erfc}\left(\frac{x}{2\sqrt{D_C^{\gamma} \cdot t}}\right) \quad (22)$$

where D_C^{γ} is the carbon diffusivity in austenite, in cm^2/sec , and the constant β is defined as,

$$\beta = \frac{\sqrt{D_C^{\gamma}}}{\sqrt{D_C^{\alpha}}} \quad (23)$$

The Φ value in Eqs. (21) and (22) can be obtained by solving the following equation, which was derived by considering mass balance at the α - γ interface,

$$F(\Phi) = \sqrt{\pi} \cdot (C_{\gamma}^{\alpha-\gamma} - C_{\alpha}^{\alpha-\gamma}) - \left[\frac{C_{\gamma}^{\alpha-\gamma} - C_{\text{bulk}}}{\frac{\Phi}{\beta} \cdot e^{\left(\frac{\Phi}{\beta}\right)^2} \cdot \operatorname{erfc}\left(\frac{\Phi}{\beta}\right)} + \frac{C_{\alpha}^{\alpha-\gamma} - C_{\text{FeO}-\alpha}}{\Phi \cdot e^{\Phi^2} \cdot \operatorname{erf}(\Phi)} \right] = 0 \quad (24)$$

which can then be used to calculate the ferrite layer thickness using Eq. (16).

Using the Wagner's equations with the consideration of interface equilibrium, namely Eqs. (14)-(15) for the temperature range of 700–774 °C and Eqs. (21)-(24) for the range of 774–907 °C to represent the diffusion processes involved at different temperatures, the ferrite layer thickness for the range of 700–907 °C can be calculated using Eq. (16), as shown by the purple solid line in Fig. 13. It is seen that it has a maximum value at 800 °C, a much smaller value at 700 °C and a very small value at 900 °C, having a similar trend to that of the experimental results shown in Fig. 1.

If the interface carbon concentration is assumed to be zero when the Wagner's equations are used, the calculated ferrite thickness as a function of temperature is shown as the shorter green dash line in Fig. 13. It is seen that the maximum ferrite thickness is now at 829 °C, and the predicted ferrite thicknesses are significant greater at all temperatures. Particularly at 900 °C, the calculated ferrite thickness is about 80 μm , much greater than the observed thickness at 900 °C of 30 μm (Fig. 1).

If the Smith's equation without considering the interface equilibrium, namely Eq. (18), is used, the calculated ferrite thicknesses as shown by the longer blue dash line in Fig. 13 became much greater beyond 774 °C, the maximum ferrite thickness temperature is moved to 859 °C, and the calculated ferrite thickness at 900 °C is even greater at about 100 μm .

If the modified Smith's equation, Eq. (20), is used to take interface equilibrium into consideration, the calculated thicknesses are also greater than those calculated using the Wagner's equation beyond 770 °C, as shown by the red dot line in Fig. 13, although the predicted ferrite thickness at 900 °C is very much reduced at about 40 μm , closer to the observed thickness of 30 μm (Fig. 1).

The calculated results shown in Fig. 13 have several indications. First, the interface carbon content significantly affects the calculated results. If this content is

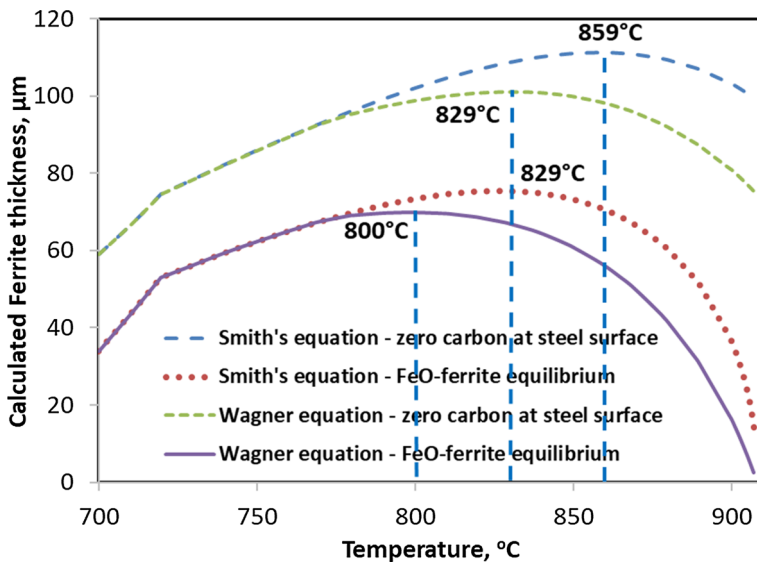


Fig. 13 Calculated ferrite thickness as a function of decarburization temperature using different equations

assumed to be zero, the calculated thicknesses are much greater at all temperatures, the calculated maximum ferrite thickness temperatures are shifted to higher temperatures, and most importantly, the trends of thickness variation with temperature deviate significantly from the observed trend shown in Fig. 1.

Second, carbon diffusion in austenite at temperatures above 774 °C affects the calculated ferrite layer thickness. Without considering this effect, namely, when the Smith equations are used, the calculated ferrite layer growth within the range of 774–900 °C can deviate from the calculated ferrite thicknesses as much as more than 15 μm. Because the formation of austenite at temperatures above the A_3 temperature for the 60Si2MnA steel examined is a reality, as seen in Fig. 11a, the use of the Smith equations is therefore inappropriate for the prediction of ferrite growth for temperatures greater than the A_3 temperature.

Thus, the most reliable calculated results are those shown by the solid purple line in Fig. 13 as reproduced as the red solid line in Fig. 14 to compare with experimental results (blue dash line). It is seen that while the predicted trend of ferrite thickness variation with temperature matches with the experimental results well, with a maximum thickness observed at around 800 °C and very small thicknesses at 700 and 900 °C, the observed ferrite thicknesses are 40 μm greater than the calculated ferrite thicknesses at around 800 °C. To obtain a perfect match, both in the trends and in the absolute values, we need to identify the reasons responsible for the thickness discrepancy near 800 °C. One reason that could be responsible is that the diffusivity data used for calculating the ferrite layer thickness could be incorrect. There are two possible causes for this.

First, in calculating the ferrite thickness using Eq. (16), the Smith's diffusivity data were used [42]. A closer examination of the technique used by Smith revealed

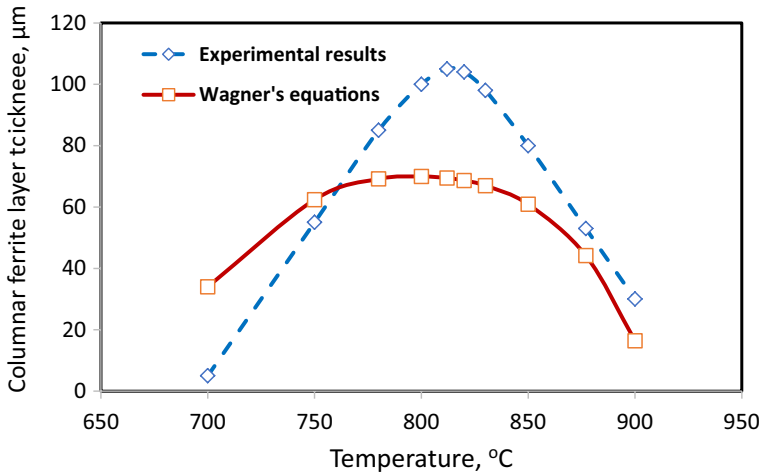


Fig. 14 Comparison of measured thicknesses of the columnar ferrite layers at different temperatures and the thicknesses calculated using the Wagner's equations assuming that the carbon concentrations are determined by interface equilibrium between FeO and dissolved carbon in the steel. The steel examined contains Fe–0.602%C–1.787%Si–0.789%Mn–0.198%Cr

that the method employed may not be reliable because Smith used Eq. (18) to compute the diffusion coefficient. As discussed earlier, in deriving Eq. (18), Smith assumed that the carbon concentration on the steel surface was zero. Such an assumption could lead to error because Smith used a H_2O-H_2 mixture produced by 'burning metered amounts of hydrogen and oxygen using a gas burner' as the decarburizing gas [42]. While the exact gas composition was not given, it was likely that the gas mixture would have a relatively high oxygen potential that corresponded to an equilibrium surface carbon concentration that was not negligible. If this was the case, then Eq. (20), rather than Eq. (18) should be used to derive the carbon diffusivity. When $C_s \neq 0$, $(C_\alpha^* - C_s)$ is always smaller than C_α^* , and therefore, a greater D_C^α value must be obtained from Eq. (20) for a given ferrite layer thickness. The actual deviation would depend on the exact gas composition applied by Smith in his experiment [42]

The second factor is the possible alloying effect on carbon diffusivity in ferrite. The steel examined in the experimental study contained 1.787%Si–0.789%Mn–0.198%Cr [28]. Based on the data presented by Krishtal, the presence of Si increases carbon diffusivity in ferrite, and the increase is more significant at higher temperatures, as shown in Fig. 15 [49]. The effect of Cr is even greater at higher temperatures (Fig. 15) [49], and there could be the combined effect of Cr and Si, which could be even more profound, similar to that observed in austenite [55]. By calculation using Eq. (16), if the true carbon diffusivity at around 800 °C is twice as large, then the predicted maximum ferrite thickness can match the observed values well. Future studies will be required to understand the true reasons of the observed discrepancy.

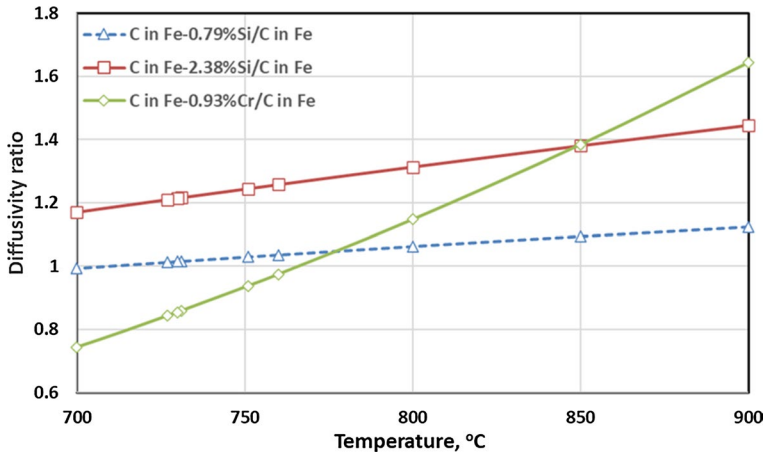


Fig. 15 Effect of Si and Cr additions on carbon diffusivity in ferrite, expressed as the ratio between the carbon diffusivity in a Fe-Si or Fe-Cr alloy and carbon diffusivity in pure iron [49]

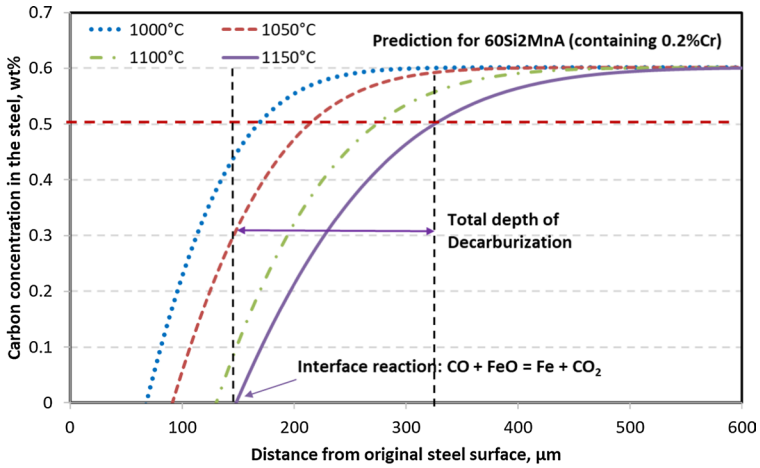
Analytical Solution for Scenario III

Applying the boundary condition specified in Fig. 12c and the initial condition of $C_{x,t} = C_C^{\gamma-bulk}$ at $x \geq 0$ at $t = 0$ to Eq. (13), one obtains: [37]

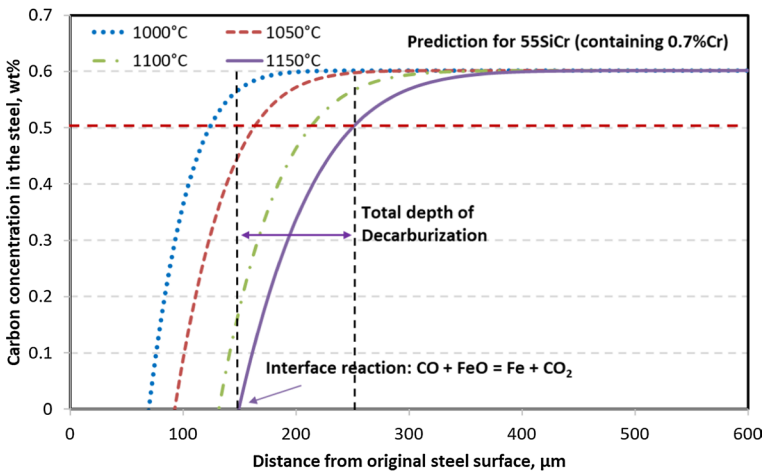
$$C_{x,t} = C_{bulk} - \frac{(C_{bulk} - C_{FeO-\gamma})}{\operatorname{erfc}\left[\frac{\sqrt{k_p}}{2\sqrt{D_C^\gamma}}\right]} \operatorname{erfc}\left[\frac{x}{2\sqrt{D_C^\gamma t}}\right] \tag{25}$$

where $C_{x,t}$ is the carbon concentration at the location x at time t and D_C^γ is the carbon diffusivity in austenite, assumed to be a constant at a certain temperature. This equation is equivalent to that derived by Birks et al. [4–7] where the scale-steel interface position is expressed as $x^2 = 2k_C t$, rather than $x^2 = k_p t$ as defined in Fig. 12, namely $k_p = 2k_C$. The assumption of parabolic scaling is convenient in arriving at a simple solution because it allows one to eliminate the time variable t from the term $\frac{x}{2\sqrt{D_C^\gamma t}} = \frac{\sqrt{k_p t}}{2\sqrt{D_C^\gamma t}} = \frac{\sqrt{k_p}}{2\sqrt{D_C^\gamma}}$, when the boundary condition $C_{x,t} = C_C^{FeO-\gamma}$ at the scale-steel interface $x = X$ is applied.

The calculated carbon concentration profiles in the partial decarburization zones in a 60Si2MnA steel 1000–1150 °C after 20 min of oxidation in wet air that contains 24.8% H₂O are shown in Fig. 16a [37]. Consistent with the experimental observations shown in Figs. 4 and 5, the calculated decarburization depth increased with increasing temperature within this range, as summarized in Table 2.



(a)



(b)

Fig. 16 Calculated carbon concentration gradients in austenite at different temperatures within the range of 1000–1150 °C: **a** for 60Si2MnA using carbon diffusivity data derived for Fe–0.2%C–1.2%Si–0.2%Cr, and **b** for 55SiCr using diffusivity data derived for Fe–0.2%C–1.2%Si–0.7%Cr (showing the combined effect of Si with a higher Cr content)

Alloying Effects on Decarburization

Effects on Carbon Diffusivity

The analytical solutions given in Eqs. (13), (14), (21), (22) and (25) were obtained under the assumption that carbon diffusivity was not a function of carbon

Table 2 Comparison of calculated and measured decarburization depth in austenite (for surface regions where carbon concentration decreased to below 0.5 wt%)

Temperature, °C	1000	1050	1100	1150
Measured depth in 60Si2MnA, μm (Figs. 4, 5)	100	125	150	180
Calculated depth for 60Si2MnA using carbon diffusivity in Fe–0.2%C–1.2%Si–0.2%Cr	97	121	142	179
Calculated depth for 55SiCr using carbon diffusivity for Fe–0.2%C–1.2%Si–0.6%Cr	57	70	64	104
Calculated depth for 60Si2MnA using carbon diffusivity calculated by Lee’s equation	259	346	417	539

concentration in the relevant phases. It is well known that the diffusivity of carbon in austenite is a function of carbon concentration [50–54]. It is also affected significantly by the presence of alloying elements [49, 55–61]. The most comprehensive equation currently available was that derived by Lee et al., [57] who incorporated the binary alloying effects provided by Krishtal: [55]

$$D_C^γ = [0.146 - 0.036C(1 - 1.075Cr)] + k_{1,Si}M_{Si} + k_{1,Mn}M_{Mn} + k_{1,Cr}M_{Cr} \cdot \exp \left[- \frac{144.3 - 15.0C + 0.37C^2 + k_{2,Si}M_{Si} + k_{2,Mn}M_{Mn} + k_{2,Cr}M_{Cr}}{R_{kj}T} \right] \tag{26}$$

where $k_{1,i}$ ($i = Si, Mn$ and Cr) and $k_{2,i}$ ($i = Si, Mn$ and Cr) are given in Table 3, and M_i ($i = Si, Mn$ and Cr) is the concentration for Si, Mn and Cr, respectively, in wt%.

However, in a closer examination, it was found that the authors had used experimental data for ternary Fe-M-C systems (M being a metallic element) only [55, 61]. More valuable data for quaternary systems Fe–1.2wt%Si–0.7%C–xCr also provided by Krishtal [55] were not incorporated in the derivation of Eq. (26). One important finding reported by Krishtal was that while Cr and Si alone had retarding effects to carbon diffusion, the combined effect of Cr and Si was much more profound, as shown in Table 4. Taking the steels containing Fe–0.7C for example. An addition of 1.6%Si decreased the carbon diffusivity by about 10%, whereas if 1.6%Si and 0.2%Cr were simultaneously added to Fe–0.7%C, the carbon diffusivity was reduced by more than six times for the temperature range of 1000–1200 °C.

The much lower carbon diffusivity can produce a much shallower decarburization depth, as shown in Table 2, which also listed the calculated results for 55SiCr shown in Fig. 16b and the calculated results for 60Si2MnA using diffusivity data calculated using Eq. (26) for comparison. It can be seen that if the calculated results

Table 3 Alloying parameters used in the Lee’s equation [58] for calculating carbon diffusivities in austenite

M	Mn	Si	Cr
M_i (wt%)	0.789	1.787	0.198
$k_{1,i}$	– 0.0315	0.0509	0.0
$k_{2,i}$	– 4.3663	4.0507	7.7260

Table 4 Carbon diffusivities in austenite from different sources D_c , cm^2/sec

Source	Alloy system, in wt%	$10^7 \times$ Carbon diffusivity, cm^2/s , at different temperatures, °C							D_p , cm^2/s	Q , J/mol
		1000	1050	1100	1150	1170	1200			
Krishnal (calculated from D_p and Q data and calibrated against experimental data)	Fe-0.2C	2.45	3.90	6.02	8.99	10.48	13.08	0.05600	130,625	
	Fe-0.7C	4.23	6.75	10.39	15.53	18.09	22.58	0.09600	130,540	
	Fe-0.2C-1.6Si	2.09	3.36	5.21	7.85	9.17	11.50	0.06000	133,050	
	Fe-0.7C-1.6Si	3.83	6.15	9.56	14.39	16.82	21.08	0.11000	133,050	
	Fe-0.2C-1Mn	2.63	4.22	6.54	9.83	11.47	14.36	0.07000	132,215	
	Fe-0.7C-1Mn	4.14	6.64	10.28	15.44	18.03	22.57	0.11000	132,215	
	Fe-0.2C-1Cr	1.42	2.34	3.73	5.74	6.76	8.58	0.08000	140,165	
	Fe-0.7C-1Cr	2.31	3.81	6.06	9.32	10.99	13.94	0.13000	140,165	
	Fe-0.7C-1.2Si-1Mn	2.45	3.89	5.98	8.91	10.37	12.92	0.05130	129,700	
	Fe-0.7C-1.2Si-0.2Cr	0.710	1.11	1.67	2.45	2.83	3.49	0.00890	124,265	
	Fe-0.7C-1.2Si-1.03Cr	0.157	0.254	0.398	0.603	0.71	0.888	0.00550	135,145	
Extrapolated*	Fe-0.2C-1.2Si-0.2Cr	0.387	0.603	0.910	1.334	1.543	1.906	0.00485	124,265	
Extrapolated*	Fe-0.7C-1.2Si-0.7Cr	0.294	0.469	0.724	1.082	1.262	1.575	0.00685	130,819	
Extrapolated*	Fe-0.2C-1.2Si-0.7Cr	0.160	0.256	0.395	0.590	0.688	0.859	0.00374	130,819	
Lee's equation	Fe-0.2C-1.8Si-0.79Mn-0.20Cr	1.99	3.36	5.45	8.56	10.17	13.04	0.20643	146,640	
	Fe-0.6C-1.8Si-0.79Mn-0.20Cr	3.28	5.43	8.65	13.33	15.72	19.97	0.19504	140,730	

* The data for the quaternary Fe-0.2C-1.2Si-(0.2-0.7)Cr systems were extrapolated from the data of the quaternary system Fe-0.7C-1.2Si-0.2Cr, Fe-0.7C-1.2Si-0.2Cr and ternary systems Fe-0.2C-1.6Si and Fe-0.7C-1.6Si systems to factor in the effects of chromium and carbon concentrations, with reference to the binary Fe-0.2C and Fe-0.7C systems and other ternary systems

using diffusivity data derived from Eq. (26) had represented the true decarburization depths when the combined effect of Cr and Si were absent, then the presence of the combined Cr-Si effect in 60Si2MnA decreases this depth by 60%. The predicted results for 55SiCr also show that by further increasing the Cr content to 0.7%, the depths can be decreased by a further 40%.

Very few experimental studies were conducted to address the effect of carbon concentration and alloying elements on the diffusivity of carbon in ferrite [62–67]. Based on available experimental data, Silva and McLellan derived an equation to calculate D_C^α : [68]

$$\ln(D_C^\alpha) = -2.087 - 1.197 \cdot \chi + 0.037\chi^2 \text{ cm}^2/\text{s} \quad (27)$$

where $\chi = \frac{10000}{T} \text{ }^\circ\text{K}^{-1}$. Because Smith data were used as the most important source for the derivation, the predicted ferrite layer growth using data calculated from Eq. (27) was essentially the same as those obtained when Smith's original data were used.

As discussed earlier, Smith's data were unlikely to be reliable because the surface carbon concentration was assumed to be zero, and even if they were reliable, they were only for carbon diffusion in Fe–C system only. For spring steels, alloying effects must be also considered, as shown in Fig. 16. The data for plotting Fig. 15 are shown in Table 5 together with data from some other alloy systems. It is seen that both Si and Cr increased the activation energy of carbon diffusion, with Cr having a more profound effect. However, because the data were obtained by an indirect method using C^{14} through intermittent carburization over the temperature range 500–800 °C, they can only be used as an indication of the alloying effects, rather than for quantitative predictions [49].

More importantly, as the combined effect of Cr and Si shown for the carbon diffusivity in austenite suggested, there could be the combined effect of Cr and Si on the carbon diffusivity in ferrite that cannot be predicted by simply adding up the separate effects of Si and Cr. If this effect is understood, the discrepancy between the observed and calculated results shown in Fig. 14 then may be resolved.

Effects of Molten Oxide Formation

The most commonly used alloying element in spring steels is silicon. It is known that silicon in steel can provide good protection to high temperature oxidation below 1170 °C, but at temperatures above 1173 °C, formation of a molten oxide phase

Table 5 Alloying effect on carbon diffusivity in ferrite [49]

Steel	D_0 , cm ² /sec	Q, kJ/mole
Fe	0.21	102.9
Fe–0.79%Si	0.43	108.8
Fe–2.38%Si	0.85	113.8
Fe–3.6%Si	2.2	122.6
Fe–0.56%Mo	2.1	120.9
Fe–2.58%Mo	20	140.2
Fe–0.93%Cr	16.4	140.6

becomes possible as the reaction product of FeSi_2O_4 and FeO , which generally coexist at the scale-steel interface during oxidation of the steel [30], as indicated in the FeO-SiO_2 phase diagram shown in Fig. 17 [69, 70]. Formation of the molten oxide drastically accelerated steel oxidation [30, 37], as shown in Fig. 6. If Fe_3O_4 can form at the scale-steel interface, the molten oxide formation temperature can be even lowered to 1140–1150 °C [71–73].

When liquid oxide formed, it can erode the steel surface piece by piece, even before the steel was completely decarburized, as seen in Fig. 18. ‘Erosion’ of the steel in this way will consume a significant part of the decarburized layer. However, some degree of partial decarburization would still be expected if the oxide can react with dissolved carbon in the steel because the carbon diffusion rate in the steel is also increased significantly if there is a loss of carbon on the steel surface. This view is supported by the observation of oxygen diffusion into the steel substrate causing internal oxidation to accompany steel erosion by the molten oxide, as seen in Fig. 19. If the more difficult oxygen diffusion could take place, so could carbon, if carbon had been lost at the scale-steel interface. Therefore, the complete absence of partial decarburization suggested that there must be some other mechanisms operating to prevent decarburization reactions at the scale-steel interface.

Thermodynamic calculation indicated that the equilibrium carbon activity at the Fe_2SiO_4 /steel interface was always significantly lower than the carbon activity in the bulk of the steel (60Si2MnA), as shown in Fig. 20 [37]. The assessments required the use of silicon activity in the steel, which was computed using Pandat™. For the 60Si2MnA steel assessed, the silicon activity is a function of temperature, given by:

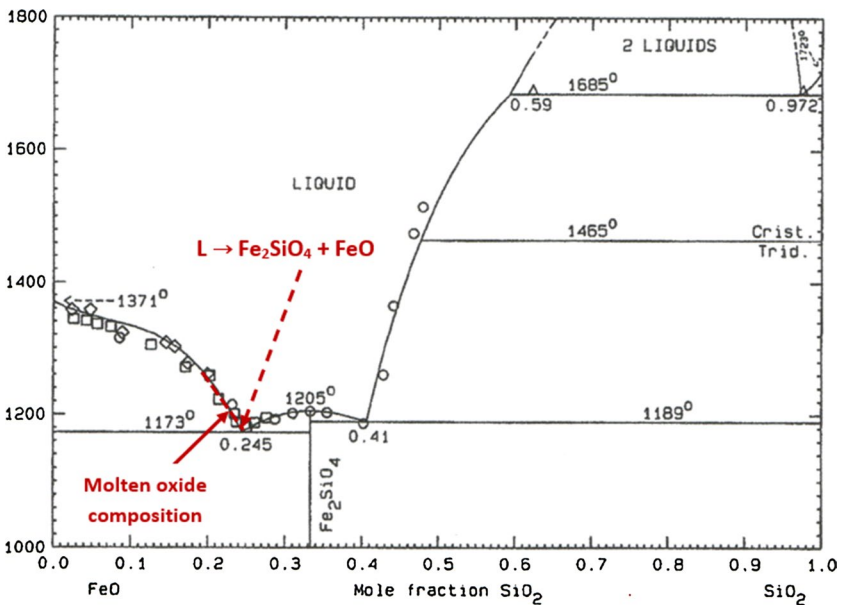


Fig. 17 FeO-SiO_2 phase diagram in the presence of iron [70, 71]

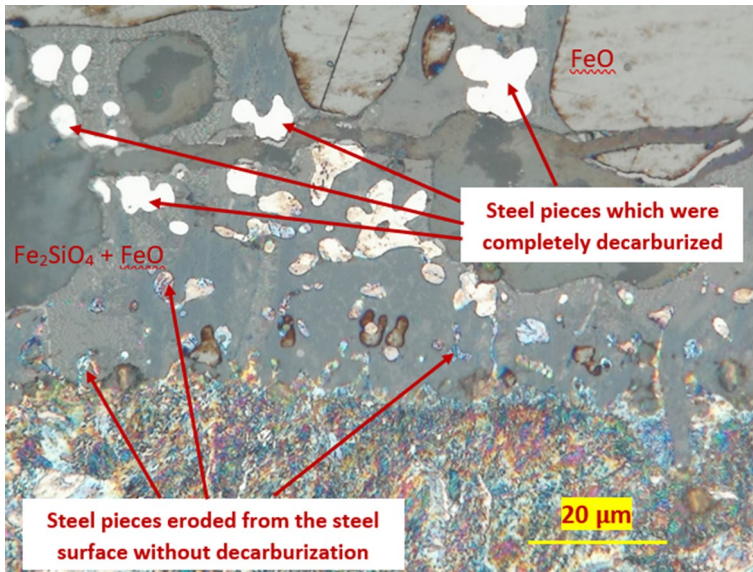


Fig. 18 Steel pieces eroded from the steel surface and encapsulated by the molten oxide after oxidation of a 60Si2MnA steel at 1190 °C in 24.8% H_2O -air for 20 min [30, 37]

$$a_{\text{Si}} = 0.255 \times e^{-\frac{116930}{RT}} \quad (28)$$

where T is temperature in K and R the gas constant in $\text{J}\cdot\text{mol}^{-1}\cdot\text{T}^{-1}$.

Different degrees of internal oxidation may consume silicon from the surface layer to different degrees, and therefore, the assessments were conducted by comparing the carbon activity in the bulk of steel and that at the interface with different degrees of remaining silicon activities, as shown in Fig. 20 [37]. The results indicated that the formation of a continuous and compact FeSi_2O_4 oxide formation on the steel surface could provide full protection from decarburization below 1084 °C. This temperature decreases with decreased level of silicon activity on the surface layer caused by internal oxidation [37].

Without the formation of a molten oxide layer, the inner scale layer was found to comprise a mixture of Fe_2SiO_4 and FeO [30] and therefore, the interface equilibrium was effectively one between FeO and the steel. When a molten oxide forms, however, the interface carbon activity is always significantly lower than that in the bulk, as seen in Fig. 20, and therefore, decarburization would be still possible if the molten oxide can react with the dissolved carbon and the reaction products CO and or CO_2 gases can escape through the molten oxide. The complete absence of decarburization thus suggested that the molten oxide was impermeable to CO and CO_2 gases. The reason could be that a liquid phase does not have micro-cracks of grain boundaries for the gases to travel through. In addition, because the molten oxide could wet both the steel and the FeO phase well, as shown in Figs. 4d–f, 18 and 19, it could then spread along the interface to cover the entire steel surface during steel oxidation, thus preventing the steel from decarburization completely.

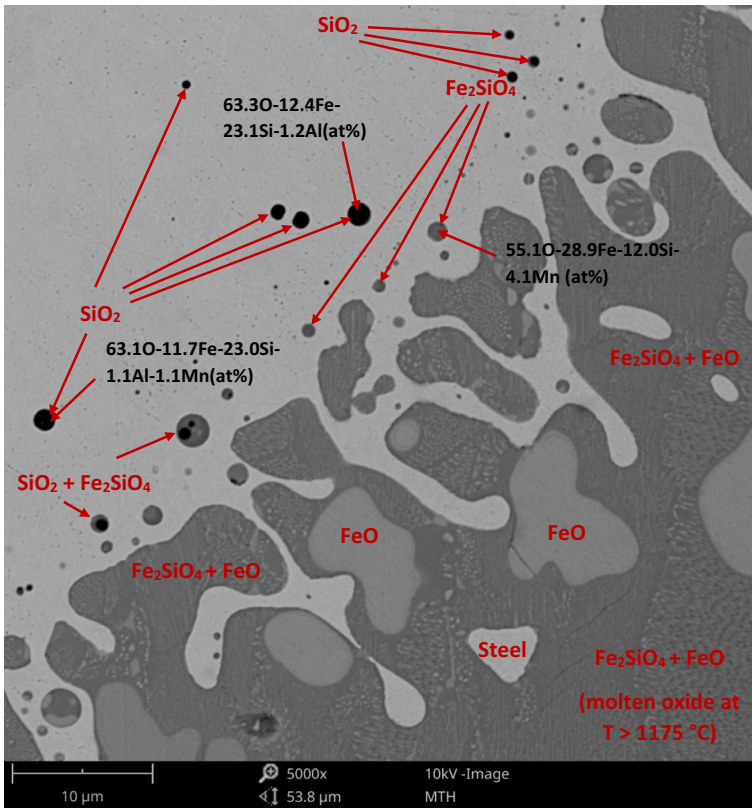


Fig. 19 SEM image of the scale-steel interface in the specimen oxidized in wet air at 1200 °C. The different phases indicated were determined by EDS analyses [30, 37]

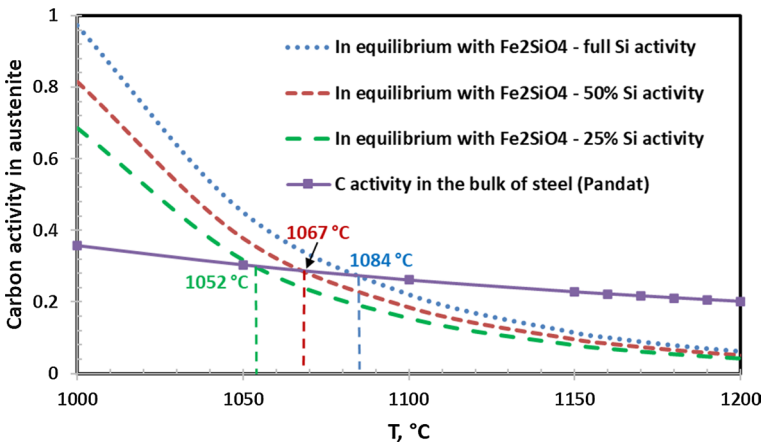
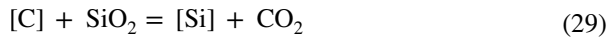


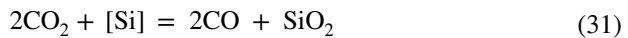
Fig. 20 Effect of Fe_2SiO_4 formation on decarburization at different levels of remaining Si activity in the surface layer of the steel caused by internal oxidation

Effect of Possible Formation of SiO₂ on the Steel Surface

One interesting finding of an earlier study was that when the 60Si2MnA steel was exposed to a dry O₂-containing atmosphere, decarburization could be prevented or eliminated with very little scale formed [28]. The observed phenomenon was attributed to the possible formation of a highly protective SiO₂ scale covering the steel surface, thus providing protection from both oxidation and decarburization. The possible reactions dominating decarburization under this condition are:



The reaction products CO₂ and CO then maintain their equilibrium with [Si] and [C] via the following reaction:



and the reaction shown in Eq. (6). The free energy of formation for Reaction (31) is:

$$\Delta G_T^0 = -306690 + 7.531T = -RT \ln \frac{P_{\text{CO}}^2}{P_{\text{CO}_2}^2 \cdot a_{\text{Si}}} \quad (32)$$

or

$$\frac{P_{\text{CO}}}{P_{\text{CO}_2}} = e^{-\left[\frac{(-306690+7.531T)}{2RT} - \frac{\ln a_{\text{Si}}}{2}\right]} \quad (33)$$

The calculated $\frac{P_{\text{CO}}}{P_{\text{CO}_2}}$ then can be used to calculate the equilibrium carbon activity using Eq. (8), which then can be converted equilibrium carbon concentration at the interface assuming that the steel is in an austenitic state using Eq. (12). Table 6 compares the calculated equilibrium carbon concentrations at the SiO₂-steel interface and that in the steel, as well as those in equilibrium with FeO and Fe₂SiO₄, for the range of 800–1250 °C. It is seen that the calculated equilibrium carbon concentrations are extremely high, much higher than that in the bulk, indicating that when a compact SiO₂ formed on the surface preventing direct contact between the steel and the atmosphere, decarburization can be prevented, as already observed [28]

Conclusions

Steel decarburization is a very old research topic and also an unresolved problem for medium and high carbon steel manufacturers. Despite the claim by Birks et al. in 1983 that the mechanism of decarburization for plain carbon and low alloy steels was already well understood, conventional theories could not explain many aspects of steel decarburization. One such aspect was the formation mechanism of a columnar ferrite layer on steel which became a hot topic recently in the study of spring

Table 6 Calculated equilibrium carbon concentrations at the oxide-steel interface covered by different types of oxides

T, °C	FeO	Solid Fe ₂ SiO ₄	Molten Fe ₂ SiO ₄	SiO ₂	Bulk of steel—aus-tenite
800	#N/A	4.788	#N/A	5.086	0.602
900	0.0548	3.490	#N/A	5.000	0.602
1000	0.0245	1.494	#N/A	4.548	0.602
1100	0.0123	0.560	#N/A	3.244	0.602
1150	0.00897	0.341	#N/A	2.376	0.602
1200	0.00670	#N/A	0.211	1.571	0.602
1250	0.00509	#N/A	0.137	#N/A	0.602

steel decarburization. This review summarizes the findings of our recent studies on this topic, particularly the development of a new decarburization theory to interpret the formation mechanism of the columnar ferrite layer, leading to the following conclusions:

- (1) A columnar ferrite layer is generally observed in the surface area of a spring steel if the steel is exposed to an oxidizing atmosphere within the temperature range of 700–900 °C. Different studies claimed different temperatures at which a maximum columnar ferrite layer thickness developed and there had been no consensus on the mechanism responsible for its formation. Our studies found that this temperature is within the range of 800–820 °C and the presence of such a maximum ferrite thickness could be explained by the new simultaneous scale reduction and steel decarburization theory we developed recently.
- (2) The new theory proposes that when a steel is covered by a FeO scale, the FeO scale, whether it is in contact or detached from the steel surface, could react with dissolved carbon in the steel, causing simultaneous reduction of the FeO scale itself and decarburization of the steel. Whether the reaction can take place or not depends on whether the carbon activity in the steel is greater than the equilibrium carbon activity at the FeO-steel interface when the surface oxides are solid which were found to be permeable to CO and CO₂. However, at temperatures above 1170 °C, formation of a liquid oxide phase is possible, which is able to spread and cover the steel surface thus preventing steel decarburization altogether.
- (3) The new theory not only satisfactorily explains the observed reduction kinetics of the FeO scale, but more importantly for this study provides a good explanation of the columnar ferrite formation phenomenon with a maximum thickness observed at 800–820 °C. The columnar ferrite structure is believed to be caused by directional growth of the ferrite phase toward to steel substrate opposite to the carbon diffusion direction as a result of gradual carbon loss from the surface of the steel, whereas the presence of a maximum ferrite thickness is the combined effect of three factors: the presence of a maximum carbon solubility in ferrite at

about 720 °C, gradual decreasing trend of the equilibrium carbon concentration at the ferrite-scale interface with temperature, and the rapid increase of carbon diffusivity in ferrite with temperature, leading to the presence of a maximum carbon permeability through the ferrite layer, which is defined as the product of the carbon concentration difference between the two interfaces of the ferrite layer and the carbon diffusivity in ferrite.

- (4) Historically in dealing with steel decarburization under oxidizing conditions, it was always assumed that the carbon concentration on the steel surface was negligible and treated as zero. Based on the new theory, this is no longer the case when the formation of a ferrite layer is possible, because within the temperature range where ferrite is stable, the magnitude of the equilibrium carbon concentration at the FeO-steel interface is in the same magnitude as that of carbon solubility in ferrite.
- (5) Incorporating the new interface conditions determined by the FeO-steel equilibrium, a set of equations for calculating carbon concentration gradient in the austenite are summarized in this study. However, it was found that there was significant discrepancy in the predicted and experimentally measured decarburization depths in austenite when the carbon diffusivity data summarized by Lee et al. were used.
- (6) Further examination of available data showing the alloying effects on carbon diffusivity revealed that in the presence of both Cr and Si in the steel, the Lee's equation should not be used as it did not consider the combined effect of these two elements.
- (7) It was also found that the diffusivity data derived by Smith may not be reliable either because Smith had used an overly simplified Wagner's equation to derive the diffusivity data. In Smith's study, the carbon concentration at the steel surface was assumed to be zero. Based on the finding of the current study, this could have led to error because the equilibrium carbon concentration on the steel surface could be in the same magnitude as the carbon solubility in ferrite.
- (8) The study also demonstrates how the theory can be applied to predict and explain decarburization tendency when the steel surface is covered by other oxides, such as Fe₂SiO₄, whether solid or molten, and SiO₂.

Supplementary Information The online version contains supplementary material available at <https://doi.org/10.1007/s11085-023-10181-3>.

Author contributions The manuscript and most of the figures and all tables were prepared by Dr YRC. Dr FZ computed thermodynamic data, assisted in the computation of the phase diagrams and assisted in the interpretation of thermodynamic principles related to the interpretation of the research results. Both authors reviewed the manuscript.

Funding There was no funding provided for this work.

Declarations

Competing interests The authors declare no competing interests.

References

1. A. Bramley and K. F. Allen, *Engineering (London)* **133**, 92 (1932).
2. J. K. Stanley, *Iron Age* **151**, 31 (1943).
3. W. A. Pennington, *Transactions of the American Society for Metals* **37**, 48 (1946).
4. N. Birks and W. Jackson, *Journal of Iron and Steel Institute* **208**, 81 (1970).
5. N. Birks, *Decarburization*, (The Iron and Steel Institute, London, 1970).
6. N. Birks and A. Nicholson, *Mathematical Models in Metallurgical Process Development*, (ISI Publication 123, The Iron and Steel Institute, London, 1970).
7. N. Birks, G. H. Meier and F. S. Pettit, *Introduction to the High-Temperature Oxidation of Metals*, 2nd edn. (Cambridge University Press, Cambridge, 2006).
8. R. N. Wright, *Steel Decarburization* (ASM Handbook, ASM International 2014).
9. J. Baud, A. Ferrier, J. Manenc, and J. Bernard, *Oxidation of Metals* **9**, 69 (1975).
10. M. Nomura, H. Morimoto, and M. Toyama, *ISIJ International* **40**, 619 (2000).
11. D. Li, D. Anghelina, D. Burzic, J. Zamberger, R. Kienreich, H. Schifferi, W. Krieger, and E. Kozeschnik, *Steel Research International* **80**, 298 (2009).
12. D. Li, D. Anghelina, D. Burzic, W. Krieger, and E. Kozeschnik, *Steel Research International* **80**, 304 (2009).
13. Y. Zhang, L. Liu, C. Zhou, and J. Xiao, *International Journal of Minerals. Metallurgy and Materials* **19**, 116 (2012).
14. C. L. Zhang, L. Y. Zhou, and Y. Z. Liu, *International Journal of Minerals. Metallurgy and Materials* **20**, 720 (2013).
15. S. Choi and S. Zwaag, *ISIJ International* **52**, 549 (2012).
16. S. Choi and Y. Lee, *ISIJ International* **54**, 1682 (2014).
17. X. Shi, L. Zhao, W. Wang, B. Zeng, L. Zhao, Y. Shan, M. Shen, and K. Yang, *Transactions of Materials and Heat Treatment* **34**, 47 (2013).
18. Y. Liu, W. Zhang, Q. Tong, and L. Wang, *ISIJ International* **54**, 1920 (2014).
19. F. Zhao, C. Zhang, Q. Xiu, Y. Tan, S. Zhang, and Y. Liu, *Materials Science Forum* **817**, 132 (2015).
20. Y. Liu, W. Zhang, Q. Tong, and Q. Sun, *International Journal of Iron and Steel Research* **23**, 1316 (2016).
21. F. Zhao, C. L. Zhang, and Y. Z. Liu, *Arch. Metall. Mater.* **61**, 1715 (2016).
22. X. Xu, K. Shen, Z. Jiang, and Y. Zhang, *Hot Working Technology* **46**, 224 (2017).
23. K. Zhang, Y. Chen, Y. Sun, and Z. Xu, *Acta Metallurgica Sinica* **54**, 1350 (2018).
24. H. Zhao, J. Gao, J. Qi, Z. Tian, H. Chen, H. Zhang, and C. Wang, *Journal of Materials Research and Technology* **15**, 1076 (2021).
25. Y. Liu and X. Liu, *Heat Treatment of Metals* **44**, 115 (2019).
26. J. Liu, B. Jiang, C. Zhang, G. Li, Y. Dai, and L. Chen, *Journal of Materials Engineering and Performance* **16**, 8677 (2022).
27. R. Y. Chen, *Oxidation of Metals* **89**, 1 (2018).
28. Y. R. Chen, X. Xu, and Y. Liu, *Oxidation of Metals* **93**, 105 (2020).
29. Y. R. Chen, F. Zhang, and Y. Liu, *Metallurgical and Materials Transactions A* **51**, 1808 (2020).
30. Y. R. Chen, Y. Liu, and C. Li, *Materials at High Temperatures* **27**, 279 (2020).
31. W. Cao, S.-L. Chen, F. Zhang, K. Wu, Y. Yang, Y.A. Chang, R. Schmid-Fetzer, and W. A. Oates, *CALPHAD: Computer Coupling of Phase Diagrams and Thermochemistry* **33**, 328 (2009).
32. PanFe, *Thermodynamic database for Fe-based alloys* (CompuTherm, LLC: Middleton WI, 2019).
33. Yisheng R. Chen, *Oxidation of Metals* **93**, 1 (2020).
34. Y. Liu, W. Zhang, Q. Tong, et al., *Heat Treatment of Metals* **42**, 143 (2017).
35. Z. W. Zhang, G. Chen, and G. L. Chen, *Acta Materialia* **55**, 5988 (2007).
36. Flemings, *Solidification Processing* (McGraw-Hill, Inc., New York, 1974).
37. Y. R. Chen, F. Zhang, Y. Liu, and H. An, *Materials at High Temperatures* **39**, 21 (2022).
38. W. A. Pennington, *Transactions of the American Society of Metals* **42**, 213 (1949).
39. F. D. Richardson and J. H. E. Jeffes, *Journal of Iron Steel Institute* **160**, 261 (1948).
40. O. Kubaschewski and C. B. Alcock, *Metallurgical Thermochemistry*, (Pergamon Press, Oxford, 1979).
41. J. A. Lobo and G. H. Gaiger, *Metallurgical Transactions A* **7A**, 1347 (1976).
42. Rodney P. Smith, *Transactions of TMS-AIME* **224**, 105 (1962).

43. T. Ellis, I. M. Davidson, and C. Bodsworth, *Journal of the Institute of Iron and Steel Institute* **201**, 582 (1963).
44. H. K. D. H. Bhadeshia, *Progress in Materials Science* **29**, 321 (1985).
45. R. Y. Chen and W. Y. D. Yuen, *Oxidation of Metals* **59**, 433 (2003).
46. C. Wagner, and W. Jost, *Diffusion in Solids, Liquids, and Gases* (Academic Press Inc., New York, NY, 1960).
47. J. H. Swisher, *Metallurgical Transactions A* **16A**, 763 (1968).
48. A. R. Marder, S. M. Perpetua, J. A. Kowalik, and E. T. Stephenson, *Metallurgical Transactions A* **16A**, 1160 (1985).
49. M. A. Krishtal, *Diffusion processes in iron alloys* (Israel Program for Scientific Translations, Jerusalem, 1970).
50. R. Collin, S. Gunnarson, and D. Thulin, *Journal of the Iron and Steel Institute* **210**, 785 (1972).
51. R. M. Asimov, *Transaction of the Metallurgical Society of AIME* **230**, 611 (1964).
52. R. P. Smith, *Acta Metallurgica* **1**, 578 (1953).
53. C. Wells, W. Batz, and R. F. Mehl, *Transaction of AIME* **188**, 553 (1950); *Journal of Metals* **2**, 553–560 (1950).
54. G. Parrish and G. S. Harper, *Production Gas Carburising*, (Pergamon Press, Oxford, New York, 1985), pp. 114–116.
55. M. A. Krishtal, *Diffusion processes in iron alloys* (Israel Program for Scientific Translations, Jerusalem, 1970).
56. S. S. Babu and H. K. D. H. Bhadeshia, *Journal of Materials Science Letters* **14**, 314 (1995).
57. S.-J. Lee, D. K. Matlock, and C. J. Von Tyne, *ISIJ International* **51**, 1903 (2011).
58. S.-J. Lee, D. K. Matlock, and C. J. Van Tyne, *Scripta Materialia* **64**, 805 (2011).
59. S. K. Roy, H. J. Grabke, and W. W. Düsseldorf, *Arch. Eisenhüttenwess* **51**, 91 (1980).
60. H. K. D. H. Bhadeshia, *Metallurgical and Materials Transactions A*, **41A**, 1605 (2010); L. S. Darken, *Transactions of AIME* **180**, 430 (1949).
61. M. E. Blanter, *Diffusion processes in austenite and hardenability of alloyed steels*, Thesis, (Moskovski Institut Stali, Moscow, 1949).
62. A. E. Lord Jr. and D. N. Beshers, *Acta Metallurgica* **14**, 1659 (1966).
63. J. K. Stanley, *Metal Transactions* **185**, 752 (1949).
64. C. G. Homan, *Acta Metallurgica* **12**, 1071 (1964).
65. A. A. Vasilyev and P. A. Golikov, *Materials Physics and Mechaics* **39**, 111 (2018).
66. R. B. McLellan and P. Chraska, *Materials Science and Engineering* **7**, 305 (1971).
67. E. Jiang and E. A. Carter, *Physical Review B* **67**, 214103–214111 (2003).
68. J. R. G. da Silva and Rex B. McLellan, *Materials Science and Engineering* **26**, 83 (1976).
69. N. L. Bowen and J. F. Schairer, *American Journal of Science. Series* **5**, 177 (1932).
70. P. Wu, G. Eriksson, A. D. Pelton, and M. Blander, *ISIJ International* **33**, 26 (1993).
71. A. Muan, *Transaction of AIME* **203**, 965 (1955); *Journal of Metals* **7**, 965 (1955).
72. A. Muan and E. F. Osborn, *Phase Equilibria among Oxides in Steelmaking*, (Addison-Wesley Publishing Company, Massachusetts, 1965).
73. V. Raghavan, in: *Phase Diagrams of Ternary Iron Alloys, Part 5: Ternary Systems Containing Iron and Oxygen*, (The Indian Institute of Metals, Calcutta, 1989), p. 260.

Publisher's Note Springer Nature remains neutral with regard to jurisdictional claims in published maps and institutional affiliations.

Springer Nature or its licensor (e.g. a society or other partner) holds exclusive rights to this article under a publishing agreement with the author(s) or other rightsholder(s); author self-archiving of the accepted manuscript version of this article is solely governed by the terms of such publishing agreement and applicable law.